CHEMISTRY OF MATERIALS
Article

Chem. Mater. **2010,** *22,* 4879–4889 4879
DOI:10.1021/cm101419w

Controllable Synthesis of Pure-Phase Rare-Earth Orthoferrites Hollow Spheres with a Porous Shell and Their Catalytic Performance for the CO + NO Reaction

Xun Li,[†] Changjin Tang,[‡] Man Ai,[†] Lin Dong,[‡] and Zheng Xu*,[†]

[†]*State Key Laboratory of Coordination Chemistry and Nanjing National Laboratory of Microstructure, School of Chemistry and Chemical Engineering, Nanjing University, Nanjing, 210093, People's Republic of China, and* [‡]*Key Laboratory of Mesoscopic Chemistry of MOE, School of Chemistry and Chemical Engineering, Nanjing University, Nanjing, 210093, People's Republic of China*

Received January 22, 2010. Revised Manuscript Received July 20, 2010

Pure perovskite $LnFeO_3$ (Ln = La, Pr−Tb) hollow spheres with porous shell and solid spheres (Ln = Dy−Yb, Y) have been successfully synthesized via calcination of a Ln-Fe citrate complex precursor, which was prepared via a convenient and effective hydrothermal method. The reaction parameters to obtain the Ln-Fe citrate complex with Ln/Fe = 1:1 can be calculated using a diagram of reaction species distribution in the solution. The calculated value was coincident well with the experimental one. The composition and the thermal decomposition processes of the Ln-Fe citrate complex were investigated carefully, using elemental analysis, inductively coupled plasma analysis (ICP), energy-dispersive spectroscopy (EDS), thermogravimetric analysis (TGA), Fourier transform infrared spectroscopy (FTIR), and X-ray diffraction (XRD). The formation mechanism of the Ln-Fe citrate complex hollow spheres was proposed as an acidic digestion ripening process. Furthermore, all 13 pure-phase $LnFeO_3$ microspheres had an excellent catalytic performance for the NO + CO reaction. The experimental results showed that the completed conversion of NO and specific selectivity of N_2 were achieved, which could be comparable with the noble metal catalysts and better than that of $LnFeO_3$ nanoparticles synthesized via the Pechini process. In addition, the $LnFeO_3$ microspheres exhibited good chemical stability and almost invariable catalytic activity during the lifetime test lasting for 96 h.

1. Introduction

The air quality of cities gets worse and worse, and both carbon monoxide (CO) and nitric oxide (NO) are considered to be the major pollutants from automobile emissions, which have caused serious environmental problems, such as acid rain, photochemical smog, respiratory diseases, and so on.[1] It would be an ideal way to eliminate both of them simultaneously via the catalytic reduction of NO by CO. Therefore, developing an excellent catalyst for this reaction is of great importance for both research and practical applications. Although many works were reported recently, most of them adopted noble metals (Rh,[2] Pt,[3] Pd,[4] Au,[5] and Ir[6]) as a catalyst. Because of the drawbacks of noble metals in practical application, including high cost, volatilization, and sintering at high temperature, the replacement of noble metals is urgently needed. Perovskite oxides, such as rare-earth orthoferrites ($LnFeO_3$), have been considered as hopeful candidates for the catalytic reduction of NO by CO and promising alternatives to noble metals.[7]

Usually, the $LnFeO_3$ compounds are prepared by heating the corresponding metal oxides in 1:1 stoichiometric ratio at high temperature.[8] However, the phase

*Author to whom correspondence should be addressed. Tel.: +86-25-83593133. Fax: +86-25-83314502. E-mail: zhengxu@nju.edu.cn.

(1) (a) Armor, J. N. *Appl. Catal., B* **1992**, *1*, 221. (b) Busca, G.; Lietti, L.; Ramis, G.; Berti, F. *Appl. Catal., B* **1998**, *18*, 1. (c) Pârvulescu, V. I.; Grange, P.; Delmon, B. *Catal. Today* **1998**, *46*, 233. (d) Roy, S.; Hegde, M. S.; Madras, G. *Appl. Energy* **2009**, *86*, 2283.
(2) (a) Kašpara, J.; de Leitenburga, C.; Fornasieroa, P.; Trovarellib, A.; Graziania, M. *J. Catal.* **1994**, *146*, 136. (b) Chafik, T.; Kondarides, D. I.; Verykios, X. E. *J. Catal.* **2000**, *190*, 446. (c) Ikeda, M.; Tago, T.; Kishida, M.; Wakabayashi, K. *Chem. Commun.* **2001**, 2512.
(3) (a) Mergler, Y. J.; Nieuwenhuys, B. E. *J. Catal.* **1996**, *161*, 292. (b) Nováková, J.; Kubelková, L. *Appl. Catal., B* **1997**, *14*, 273.
(4) (a) Rainer, D. R.; Vesecky, S. M.; Koranne, M.; Oh, W. S.; Goodman, D. W. *J. Catal.* **1997**, *167*, 234. (b) Holles, J. H.; Davis, R. J.; Murray, T. M.; Howe, J. M. *J. Catal.* **2000**, *195*, 193. (c) Pisanu, A. M.; Gigola, C. E. *Appl. Catal., B* **1999**, *20*, 179.
(5) (a) Mellor, J. R.; Palazov, A. N.; Grigorova, B. S.; Greyling, J. F.; Reddy, K.; Letsoalo, M. P.; Marsh, J. H. *Catal. Today* **2002**, *72*, 145. (b) Ilieva, L.; Pantaleo, G.; Ivanov, I.; Venezia, A. M.; Andreeva, D. *Appl. Catal., B* **2006**, *65*, 101. (c) Ilieva, L.; Pantaleo, G.; Ivanov, I.; Nedyalkova, R.; Venezia, A. M.; Andreeva, D. *Catal. Today* **2008**, *139*, 168.
(6) (a) Ogura, M.; Kawamura, A.; Matsukata, M.; Kikuchi, E. *Chem. Lett.* **2000**, 146. (b) Haneda, M.; Yoshinari, T.; Sato, K.; Kintaichi, Y.; Hamada, H. *Chem. Commun.* **2003**, 2814. (c) Wang, A.; Ma, L.; Cong, Y.; Zhang, T.; Liang, D. *Appl. Catal., B* **2003**, *40*, 319.
(7) (a) Libby, W. F. *Science* **1971**, *171*, 499. (b) Tabata, K.; Misono, M. *Catal. Today* **1990**, *8*, 249. (c) Viswanathan, B. *Catal. Rev.−Sci. Eng.* **1992**, *34*, 337. (d) Mizuno, N.; Tanaka, M.; Misono, M. *J. Chem. Soc. Faraday Trans.* **1992**, *88*, 91. (e) Lindstedt, A.; Strömberg, D.; Abul Milh, M. *Appl. Catal., A* **1994**, *116*, 109. (f) Simonot, L.; Garin, F.; Maire, G. *Appl. Catal., B* **1997**, *11*, 181. (g) Shen, S.-T.; Weng, H.-S. *Ind. Eng. Chem. Res.* **1998**, *37*, 2654. (h) Zhu, J.; Thomas, A. *Appl. Catal., B* **2009**, *92*, 225.

Published on Web 08/05/2010

structures of the products obtained from high-temperature reactions are generally thermodynamically stable garnets ($Ln_3Fe_5O_{12}$), rather than metastable perovskites ($LnFeO_3$). Besides solid-state calcination, $LnFeO_3$ nanoparticles or nanocrystals have been synthesized via various wet-chemistry methods (for instance, sol−gel method,[9] polyol method,[10] Pechini process,[11] and combustion route[12]). Since no intrinsic positional control is offered in the starting materials, the lanthanide and iron compounds present randomly in the solution, and the coexistence of undesired phases (e.g., $Ln_3Fe_5O_{12}$ and Fe_3O_4) or phase segregation, is inevitable.[9a,10] Recently, mixed metal-organic precursors and heterobimetallic single molecular precursors were introduced to synthesize rare-earth orthoferrites, in which the inherent control of stoichiometry ensured the purity of the product.[13] Mathur and co-workers obtained nanocrystalline $GdFeO_3$ and $YFeO_3$ without any garnet impurity using a type of single molecular precursor $[GdFe(OPr^i)_6(HOPr^i)]_2$ and $[YFe(OPr^i)_6(HOPr^i)]_2$, respectively.[13a,b] Zhang's group synthesized a series of nanocrystalline $LnFeO_3$ using heterobimetallic colloidal precursors, which were prepared by heating Ln-oleate and Fe-oleate in 1-octadecene at 320 °C for 2 h.[13c] However, the nanocrystalline $LnFeO_3$ prepared via these methods is too small to prevent corrosion or aggregation during high-temperature catalytic reaction; also, the synthesis procedure of the heterobimetallic precursor is troublesome and has high cost. Therefore, a convenient and effective method to fabricate pure-phase and shaped architectures of $LnFeO_3$ in microscale is deemed urgent.

To this end, we have established a convenient and effective method for the synthesis of pure perovskite $LnFeO_3$ microspheres with porous structure. The method contains two steps: first, the Ln-Fe citrate complex, as the precursor, is prepared via a hydrothermal process, followed by calcination in air to obtain $LnFeO_3$ (Ln = La, Pr−Tb) hollow spheres with a porous shell and solid spheres (Ln = Dy−Yb, Y), respectively. Citric acid is a common and good chelating agent for metal ions to form a coordination complex. Iron citrate and lanthanide citrate coordination polymers can be synthesized via hydrothermal reaction easily.[14] To ensure that the Ln/Fe ratio is 1:1 in the precursor, it is a key point to adjust the concentration of the citric acid in the reaction solution accurately, because the stability constants of iron citrate complex and a series of lanthanide citrate complexes are different from each other. Therefore, the diagram of the distribution of the iron and lanthanide citrate complexes, as a function of the concentration of citric acid, was constructed, and the calculated value from the diagram will be compared with the experimental result. The formation mechanism of the $LnFeO_3$ (Ln = La, Pr−Tb) hollow spheres was also proposed. Furthermore, the catalytic performance of various $LnFeO_3$ microspheres for reduction of NO by CO was evaluated and compared with the $LnFeO_3$ nanoparticles synthesized via the Pechini process.

2. Experimental Section

2.1. Synthesis. All the chemicals were analytical grade and were used without further purification. All the lanthanide nitrates were purchased from Alfa Aesar. $Fe(NO_3)_3 \cdot 9H_2O$ and citric acid monohydrate were purchased from the Shanghai Chemical Reagent Company. In a typical synthesis, 0.24−0.28 g of lanthanide nitrate hydrate (25 mM) (the actual amount was calculated for each lanthanide nitrate) and 0.252 g of $Fe(NO_3)_3 \cdot 9H_2O$ (25 mM) were dissolved into 25 mL of deionized water under magnetic stirring. After stirring for 30 min, a certain amount of citric acid monohydrate (70−150 mM, depending on the type of lanthanide) was added to the above solution. After stirring for another 30 min, the solution was transferred into a 30-mL stainless autoclave, sealed, and heated at 180 °C for 24 h. After that, the autoclave was cooled to room temperature naturally and the brown precipitate (precursors, Ln-Fe citrate complex) were separated by centrifugation, washed with deionized water and absolute ethanol and dried at 80 °C, then heated in air at 800 °C for 2 h to obtain $LnFeO_3$ microspheres. For the Pechini process, 1 mmol of lanthanide nitrate hydrate and 1 mmol of $Fe(NO_3)_3 \cdot 9H_2O$ were dissolved into 50 mL of deionized water under magnetic stirring. Then, 4 mmol of citric acid monohydrate and 12 mmol of ethylene glycol were added into the above solution under magnetic stirring at 80 °C. After the water was evaporated, the viscous gels were dried at 150 °C for 24 h, followed by calcination at 800 °C for 2 h.[11c]

2.2. Characterization. All products were imaged with a Hitachi Model S-4800II field emission scanning electron microscopy (FESEM) system that was equipped with an AMETEK energy-dispersive X-ray spectroscopy (EDS) device to get FESEM images and EDS patterns. Transmission electron microscopy

(8) (a) Sztaniszlav, A.; Sterk, E.; Fetter, L.; Farkas-Jahnke, M. *J. Magn. Magn. Mater.* **1984**, *41*, 75. (b) Mathur, S.; Shen, H.; Lecerf, N.; Kjekshus, A.; Fjellvag, H.; Goya, G. F. *Adv. Mater.* **2002**, *14*, 1405. (c) Zanatta, S. C.; Cotica, L. F.; Paesano, A.; Medeiros, S. N.; Cunha, J. B. M.; Hallouche, B. *J. Am. Ceram. Soc.* **2005**, *88*, 3316. (d) Henkes, A. E.; Bauer, J. C.; Sra, A. K.; Johnson, R. D.; Cable, R. E.; Schaak, R. E. *Chem. Mater.* **2006**, *18*, 567.

(9) (a) Vaqueiro, P.; López-Quintela, M. A. *Chem. Mater.* **1997**, *9*, 2836. (b) Shabbir, G.; Qureshi, A. H.; Saeed, K. *Mater. Lett.* **2006**, *60*, 3706. (c) Yang, Z.; Huang, Y.; Dong, B.; Li, H.-L. *Mater. Res. Bull.* **2006**, *41*, 274.

(10) (a) Siemons, M.; Leifert, A.; Simon, U. *Adv. Funct. Mater.* **2007**, *17*, 2189. (b) Söderlind, F.; Fortin, M. A.; Petoral, R. M., Jr.; Klasson, A.; Veres, T.; Engström, M.; Uvdal, K.; Käll, P.-O. *Nanotechnology* **2008**, *19*, 085608.

(11) (a) Kakihana, M.; Yoshimura, M. *Bull. Chem. Soc. Jpn.* **1999**, *72*, 1427. (b) Lin, J.; Yu, M.; Lin, C.; Liu, X. *J. Phys. Chem. C* **2007**, *111*, 5835. (c) Gaki, A.; Anagnostaki, O.; Kioupis, D.; Perraki, T.; Gakis, D.; Kakali, G. *J. Alloy Compd.* **2008**, *451*, 305. (d) Yoshino, M.; Kakihana, M.; Cho, W. S.; Kato, H.; Kudo, A. *Chem. Mater.* **2002**, *14*, 3369. (e) Goldwasser, M. R.; Rivas, M. E.; Pietri, E.; Pérez-Zurita, M. J.; Cubeiro, M. L.; Gingembre, L.; Leclercq, L.; Leclercq, G. *Appl. Catal., A* **2003**, *255*, 45. (f) Natile, M. M.; Poletto, F.; Galenda, A.; Glisenti, A.; Montini, T.; De Rogatis, L.; Fornasiero, P. *Chem. Mater.* **2008**, *20*, 2314. (g) Hammami, R.; Aïssa, S. B.; Batis, H. *Appl. Catal., A* **2009**, *353*, 145.

(12) (a) Wu, L.; Yu, J. C.; Zhang, L.; Wang, X.; Li, S. *J. Solid-State Chem.* **2004**, *177*, 3666. (b) Bedekar, V.; Jayakumar, O. D.; Manjanna, J.; Tyagi, A. K. *Mater. Lett.* **2008**, *62*, 3793.

(13) (a) Mathur, S.; Shen, H.; Lecerf, N.; Kjekshus, A.; Fjellvag, H.; Goya, G. F. *Adv. Mater.* **2002**, *14*, 1405. (b) Mathur, S.; Veith, M.; Rapalaviciute, R.; Shen, H.; Goya, G. F.; Martins, W. L.; Berquo, T. S. *Chem. Mater.* **2004**, *16*, 1906. (c) Xu, H.; Hu, X.; Zhang, L. *Cryst. Growth Des.* **2007**, *7*, 1256.

(14) (a) Field, T. B.; McCourt, J. L.; McBryde, W. A. E. *Can. J. Chem.* **1974**, *52*, 3119. (b) Martin, R. B. *J. Inorg. Biochem.* **1986**, *28*, 181. (c) Baggio, R.; Perec, M. *Inorg. Chem.* **2004**, *43*, 6965. (d) Liu, S. G.; Liu, W.; Zuo, J. L.; Li, Y. Z.; You, X. Z. *Inorg. Chem. Commun.* **2005**, *8*, 328. (e) Vanhoyland, G.; Pagnaer, J.; D'Haen, J.; Mullens, S.; Mullens, J. *J. Solid State Chem.* **2005**, *178*, 166. (f) Li, F.-Y.; Xu, L.; Gao, G.-G.; Fan, L.-H.; Bi, B. *Eur. J. Inorg. Chem.* **2007**, 3405.

(TEM) images were obtained on a JEOL Model JEOL-200CX TEM system. High-resolution microscopy images were recorded on a JEOL Model JEOL-2100 high-resolution transmission electron microscopy (HRTEM) system. The phase purity of the products were characterized by powder X-ray diffraction (XRD) (Shimadzu Model XRD-6000 X-ray diffractometer with Cu Kα radiation, $\lambda = 0.15406$ nm). Inductively coupled plasma−atomic emission spectrometry (ICP-AES) measurements were completed on a Perkin−Elmer Model 5300DV apparatus. The elemental analysis of the complex precursor was conducted on Elementar Vario MICRO. Fourier transform infrared (FTIR) spectra were recorded on a VECTOR 22 device from Bruker. Thermogravimetric analysis (TGA) was performed (TA Instruments, Model SDT 2960) in flowing N_2 with a heating rate of 5 °C/min. The Brunauer−Emmett−Teller (BET) specific area was measured by a Micromeritics Model ASAP-2020 nitrogen adsorption apparatus.

2.3. Catalytic Tests. The catalytic activity test of $LnFeO_3$ for the NO + CO reaction was conducted in a quartz glass tubular reactor under atmospheric pressure that was equipped with a temperature-programmed controller. Briefly, a mixture of reactants with a NO:CO:He ratio of 5:10:85 (by volume) was passed through a catalyst bed containing 50 mg of the catalyst (40−60 mesh). The catalyst was pretreated in a N_2 stream at 100 °C for 1 h and then cooled to room temperature; then, the gas reactants were switched on. The total flow rate was 10 mL/min, and the space velocity was calculated to be ∼24 000 h^{-1}. Analysis of the reactants and products was carried out using a gas chromatograph equipped for thermal conductivity detection (TCD) and connected to a personal computer (PC) for data acquisition. A valve control via the PC enabled the sampling of 1 cm^3 of reactants and products for analysis, using a two-column system: column A with Molecular Sieve 5A and 13X (40−60 M) for separating N_2, NO, and CO, and column B with Porapak Q for separating N_2O and CO_2. All the catalysts were tested in the temperature region of 100−500 °C, and the conversion of NO and selectivity of N_2 were calculated.

3. Results and Discussion

3.1. Preparation of Rare-Earth Iron Citrate Complex Precursor. After hydrothermal treatment, a brown precipitate from the solution was obtained. A typical low-magnification SEM image of the as-synthesized La−Fe citrate complex is shown in Figure 1a, which displays dispersed microspheres (average diameter of ∼2−5 μm) with many pores on their surfaces. Closer observation (Figure 1a, inset) indicates that the surface of the microspheres is comprised of many small particles and the pores on the surface are ∼50−250 nm in diameter. The TEM image of these microspheres shown in Figure 1b demonstrates their hollow feature. The shell thickness of these hollow spheres, estimated from Figure 1b, is ∼200 nm, and the pore size measured from TEM image agrees well with the SEM result. The XRD pattern of the precursor is featureless, indicating the noncrystalline or amorphous nature of this Ln-Fe citrate complex.

As is well-known to all, citrate is a good chelating agent and can complex with Fe or Ln ions to form a 1:1 metal ion:citrate complex.[14] To obtain pure perovskite $LaFeO_3$ via calcination of the La−Fe citrate complex, the La and Fe ions must maintain equal stoichiometry in the precursor.

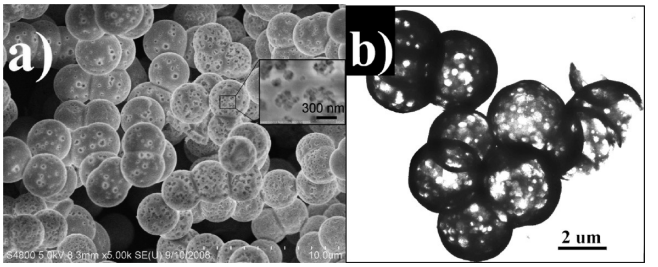

Figure 1. (a) FESEM image and (b) TEM micrograph of La−Fe citrate complex precursor.

However, the stability constants of the iron citrate complex and the lanthanum citrate complex are different, so knowledge of the variation process of the concentration of iron and lanthanide citrate complexes with the concentration of citric acid is needed. Using the software "Speciation—Calculation and Display", which is an additional part of "Demonstration Copy of the IUPAC Stability Constants Database",[15] and inputting an average pH value of 2.1 (ca. 90 mM of citric acid), the concentration of La and Fe ions (25 mM for each), and the known stability constants of citric acid, iron citrate complex and lanthanum citrate complex (the details of the stability constants of every complexes are available in Table S1 in the Supporting Information), the diagram of concentration distribution of iron and lanthanum citrate complexes, as a function of citrate concentration, was obtained (see Figure 2). Figure 2 shows that there are four citrate species in the solution, namely, iron citrate complex (FeCit, where Cit = $C_6H_5O_7^{3-}$), lanthanum citrate complex (LaCit), citric acid (H_3Cit), and dihydrogen citrate (H_2Cit^-), and the concentration of each species varies with the concentration of citrate used initially. For example, when the concentration of citric acid totally used is 50 mM, there is 50% citrate (25 mM) in iron citrate complex and ∼35% (17.5 mM) in lanthanum citrate complex, others in H_3Cit (∼13%) and H_2Cit^- (∼2%), viz, almost all Fe^{3+} (25 mM) in starting materials is transformed to iron citrate complex, whereas only 17.5 mM of La^{3+} into lanthanum citrate complex, although the amounts of Fe^{3+} and La^{3+} are the same (25 mM) in the starting materials. By further increasing the concentration of citric acid to 150 mM, it can be seen from Figure 2 that ∼17% citric acid (∼25 mM) is transformed to iron citrate complex and another ∼17% is transformed to lanthanum citrate complex, namely, all of Fe^{3+} (25 mM) and La^{3+} (25 mM) are transformed to the citrate complex, and the numbers of moles of iron and lanthanum in the citrate complexes are equivalent when the concentration of citric acid is 150 mM.

The above results given from the diagram agree very well with the experimental data from the ICP-AES analysis. As shown in Table 1, when the starting concentration of citric acid is 50 mM, little Fe^{3+} is found in the supernatant (∼9 μM) after the hydrothermal process, which

(15) The software of "Demonstration copy of the IUPAC Stability Constants Database" was downloaded from http://www.acadsoft.co.uk. Copyright: L. D. Pettit, Academic Software.

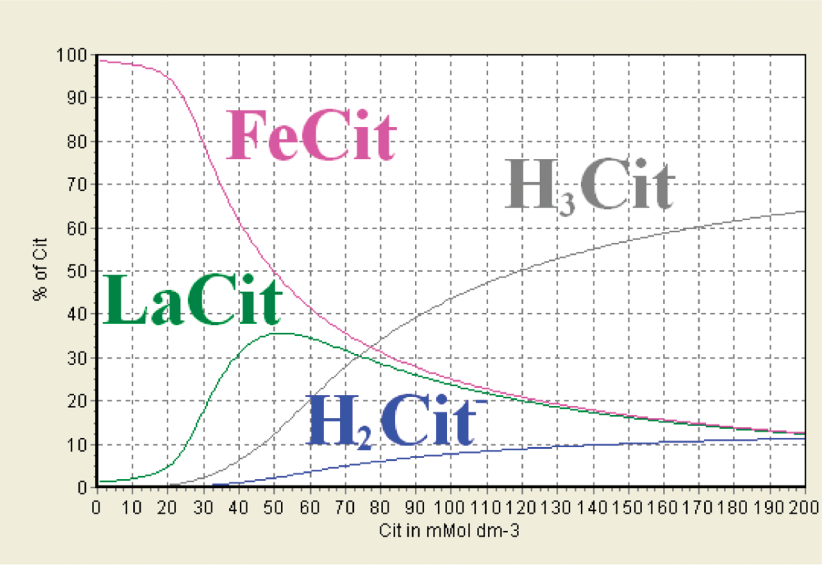

Figure 2. Distribution of iron and lanthanum citrate complexes, as a function of citrate concentration (Cit = citrate, $C_6H_5O_7^{3-}$), given from the software "Speciation—Calculation and Display".

Table 1. Concentration of Fe^{3+} and La^{3+} in the Supernatant with Different Citric Acid Concentration after Hydrothermal Reaction for 24 h

	50 mM citric acid	150 mM citric acid	300 mM citric acid	450 mM citric acid
$[Fe^{3+}]$ (mM)	9×10^{-3}	3.23	12.44	17.77
$[La^{3+}]$ (mM)	8.82	2.97	5.81	10.10

Table 2. Weight Percentage of Each Element (Calculated Value, According to the Proposed Molecular Formula and Experimental Results)

	Amount (wt %)				
	La	Fe	C	H	molecular weight
experimental	21.6[a]	8.30[a]	20.41[b]	2.61[b]	643.08
proposed	21.54	8.66	22.34	2.82	645.04

[a] Results from ICP-AES. [b] Results from elemental analysis.

means all of Fe^{3+} is transformed to the iron citrate complex, whereas 8.82 mM of La^{3+} is present in the supernatant, which matches well with the calculated value (~17.5 mM) in the lanthanum citrate complex, because the total amount of La^{3+} in the starting solution is 25 mM. When the starting concentration of citric acid is 150 mM, the concentrations of Fe^{3+} and La^{3+} in the supernatant are 3.23 mM and 2.97 mM, respectively. The reason for the residual Fe^{3+} and La^{3+} in the supernatant will be given in the following section. Nevertheless, the equivalent amounts of Fe^{3+} and La^{3+} in the supernatant indicate that the ratio of La/Fe is 1:1 in the precursor.

Furthermore, the number of moles of Fe and La ions in the precipitates of the La−Fe citrate complex in the same reaction was also measured by ICP-AES (see Table 2). The results show that the atomic ratio of these two elements is 0.96 when the starting concentration of citric acid is 150 mM, which indicated that the amounts of iron and lanthanum are almost equivalent. The composition of the La−Fe citrate complex was further confirmed by the EDS result (see Figure S1 in the Supporting Information), in which the La:Fe atomic ratio agrees well with that from ICP-AES. The elemental analysis results of the La−Fe citrate complex showed that the weight percentages of carbon and hydrogen are 20.41 and 2.61, respectively. Based on these results and combined with the earlier research on the lanthanum citrate complex,[14c−f] the La−Fe citrate complex synthesized here was proposed as a coordination polymer ($[LaFe(C_6H_5O_7)_2 \cdot 4H_2O]_n$). Weight percentages of each element in the proposed molecular formula and experimental results are in good agreement and are listed in Table 2. It can be seen that the weight percentages of carbon and hydrogen are slightly lower than that of the proposed one, which may result from the incomplete burning of the complex in the measurement. More evidence supporting the proposed molecular formula is given in the following section.

3.2. Preparation of Rare-Earth Orthoferrite Hollow ($LnFeO_3$) Spheres. $LnFeO_3$ hollow spheres were prepared via simple calcination of the rare-earth iron citrate complex precursor in air. As an example, the La−Fe citrate complex was discussed. The typical low-magnification FESEM image of the $LaFeO_3$ hollow spheres is shown in Figure 3a. The size of these spheres is in the range of 2−5 μm, which is similar to their precursor spheres and shows that the heating process has little influence on the morphology of the spheres. As shown in Figure 3b, most of the spheres are porous, with the pore diameters being ~80−300 nm on their surfaces, which is somewhat bigger than that of the precursor spheres, because of the thermal decomposition of the organic compounds. The magnified image shows that the nanoparticles constructing the surface are ~20−50 nm in size and many mesopores exist in the interstice among them (see Figure 3b, inset). Figures 3c and 3d are typical TEM images of the $LaFeO_3$ hollow spheres, which further demonstrate the hollow feature of the spheres. The insets of Figures 3c and 3d show that the shell is 40−60 nm thick and composed of nanoparticles. The HRTEM image shown in Figure 3e is taken from the shell of a hollow sphere and indicates that

the nanoparticles on the shell are highly crystallized. The 0.35 and 0.39 nm lattice spacings respectively correspond to the (111) and (110) planes of the perovskite-structured $LaFeO_3$, and the angle measured between these two planes is ca. 63°, which is in good agreement with the calculated value. The HRTEM image taken from another region (Figure 3f) also gives evidence that the nanoparticles on the shell are perovskite $LaFeO_3$ with high crystallinity. Two planes with a lattice spacing of 0.32 nm have an included angle of 49° and can be indexed to (012) and (102) planes. The XRD pattern of the product obtained by calcination of the La−Fe citrate complex precursor in air was shown in Figure 4a, in which all the peaks can be unambiguously indexed to the perovskite-structured $LaFeO_3$ and are in good accordance with the Joint Committee on Powder Diffraction Standards (JCPDS) data (Powder Diffraction File No. 74-2203). No peak belonging to La_2O_3 or Fe_2O_3 was found, which indicates that phase segregation did not happen.

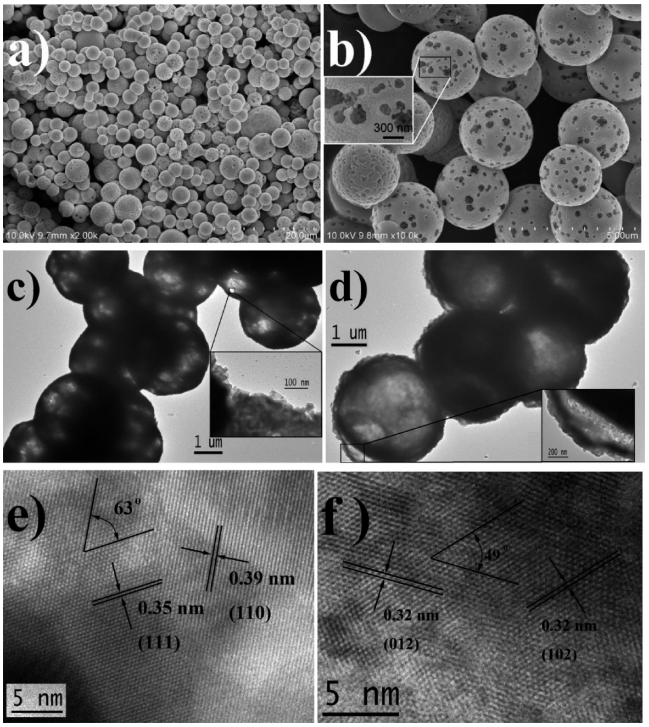

Figure 3. (a, b) FESEM images, (c, d) TEM images, and (e, f) HRTEM images of $LaFeO_3$ hollow spheres.

To investigate the evolution process from the La−Fe citrate complex precursor to perovskite-structured $LaFeO_3$, TGA, FTIR, and XRD analyses were employed. The TGA and differential thermogravimetry (DTG) curves of the precursor (Figure 4b) show that the thermal decomposition process proceeds via four stages under a N_2 atmosphere. According to the weight loss in each stage and the previous research on the thermal decomposition of the lanthanum citrate complex,[16] the process of thermal decomposition of La−Fe citrate complex was proposed and shown in Scheme 1. At the first stage, a 10.9% weight loss from 120 to 350 °C is observed, which is attributed to the loss of crystallization water. The second stage, at

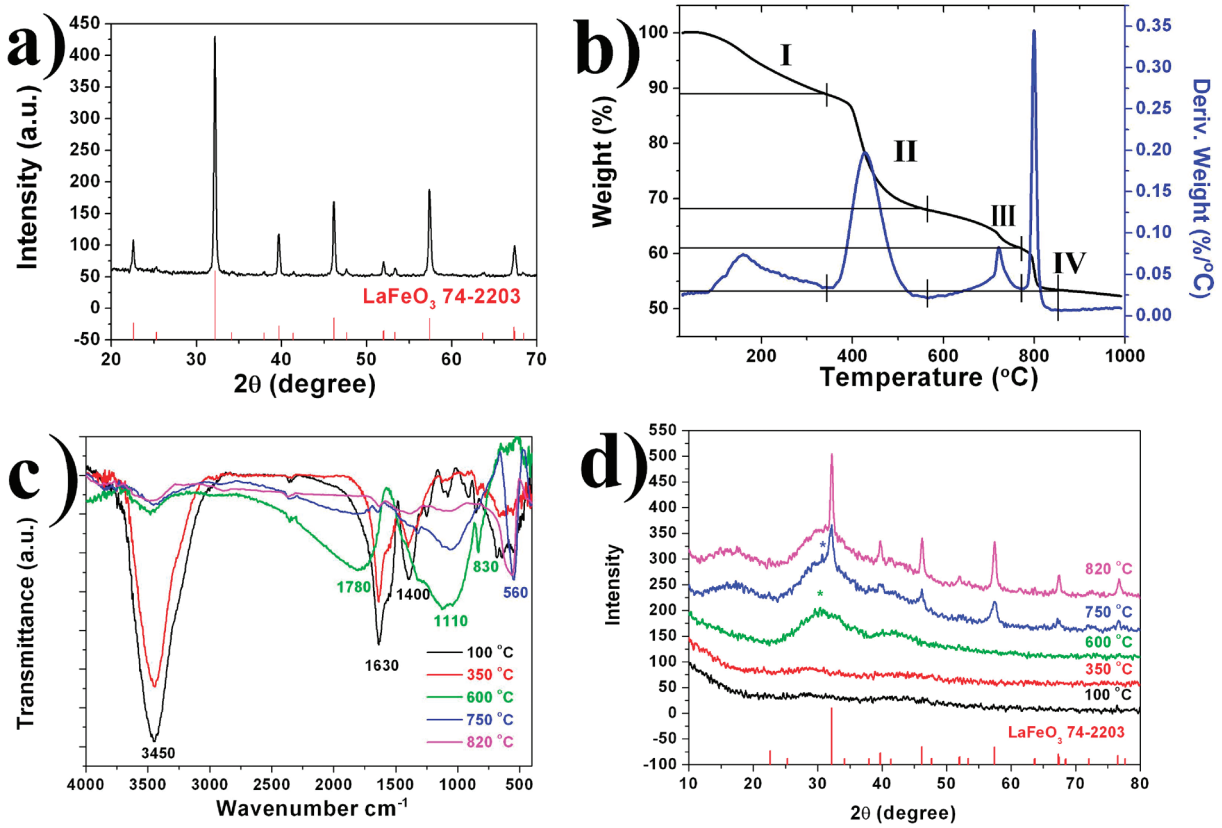

Figure 4. (a) XRD patterns of $LaFeO_3$ hollow spheres obtained via calcination of the La−Fe citrate complex precursor in air; (b) thermogravimetric profiles of La−Fe citrate complex precursor; (c) IR spectra; and (d) XRD patterns of the precursor heated at different temperatures under a N_2 atmosphere.

Scheme 1. Supposed Route of Thermal Decomposition of the La−Fe Citrate Complex Precursor

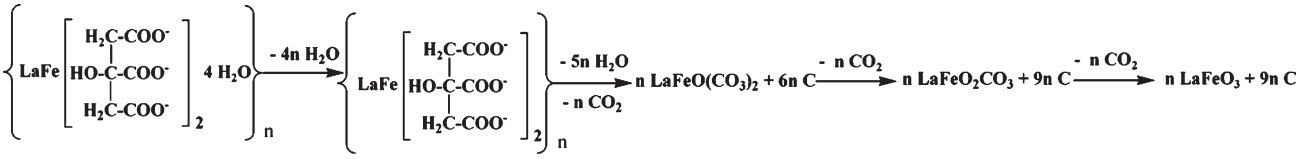

Table 3. Some Quantitative Data for the Thermal Decomposition of the La−Fe Citrate Complex Precursor (at Various Decomposition Temperatures)

	< 350 °C	425 °C	720 °C	800 °C	Total
separated products	$4H_2O$	$5H_2O + CO_2$	CO_2	CO_2	
$\Delta m/m$ (%)					
experimental	10.9	21.1	6.8	7.5	46.3
calculated	11.17	20.78	6.82	6.82	45.59

~425 °C, with a 21.1% weight loss, can be due to the oxidation of citrate to oxycarbonates via itaconates or aconitates. The third stage, from 580 °C to 760 °C, has a 6.8% weight loss, which could be suggested as being the decomposition of oxycarbonates. The last weight loss, of ca. 7.5%, happens at 800 °C, which is attributed to the further decomposition of oxycarbonates and crystallization of $LaFeO_3$. The details of the thermal decomposition of the La−Fe citrate complex precursor are listed in Table 3, and the experimental results coincide well with the calculated results. The TGA−DTG curves of the complex precursor gave strong evidence that the proposed molecular formula was reasonable.

The thermal decomposition process was also traced by FTIR spectroscopy (see Figure 4c). To do so, the La−Fe citrate complex was heated at different temperatures under a N_2 atmosphere for 10 min and then IR spectra were recorded. The complex precursor dried at 100 °C has three main peaks: a broad peak centered at 3450 cm^{-1}, which is attributed to the crystallization water, and two peaks, at 1630 cm^{-1} and 1400 cm^{-1}, that originate from the symmetric and asymmetric stretching of carboxyl root, respectively; these observations also give evidence that the carboxyl groups in the citrate are deprotonated and coordinated with the metal ion.[9a,14c−f] After annealing at 350 °C, the complex lost crystallization water and the broad peak at 3450 cm^{-1} became smaller, while the peaks belong to carboxyl root remain. The IR spectra of the sample annealed at 600 °C are quite different from that at 350 °C, in which three new peaks—centered at 1780, 1100, and 830 cm^{-1}, belonging to carbonates—appear and the peak of hydroxyl at 3450 cm^{-1} becomes much smaller, because of the further dehydration of citrate.[9a,16b,17] The IR spectra at 750 °C are similar to that at 600 °C, except the M−O band at 560 cm^{-1} appears.[9a,17] Further annealing of the sample at 820 °C makes all the IR peaks weaker, except for the M−O band at 560 cm^{-1}.

The XRD patterns of the precursor heated via the same annealing process as IR spectra tracing also give evidence to support the suggested thermal decomposition route (see Figure 4d). There is no peak in the XRD pattern of the precursor heated below 350 °C, indicating the noncrystalline or amorphous nature of the La−Fe citrate complex. After annealing at 600 °C under N_2 atmosphere, the sample has two broad peaks, at $2\theta \approx 31°$ and 44°, which belong to amorphous carbon (JCPDS Powder Diffraction File Card No. 46-0945). (The pure perovskite $LaFeO_3$ was prepared by heating the precursor in air to burn out all the carbon.) There is also a small peak at $2\theta = 31°$, which is close to the strongest peak of $La_2O(CO_3)_2$ (JCPDS Powder Diffraction File Card No. 41-0672). It can be observed that the XRD pattern of $LaFeO_3$ (JCPDS Powder Diffraction File Card No. 74-2203) appears until the annealing temperature reaches 750 °C, but also a small peak centered at 30.7° can be found, which is close to the strongest peak of $La_2O_2CO_3$ (JCPDS Powder Diffraction File Card No. 84-1963). After annealing at 820 °C, the sample becomes pure perovskite $LaFeO_3$. Although there is no standard XRD pattern of $LaFeO(CO_3)_2$ or $LaFeO_2CO_3$, the XRD patterns of $La_2O(CO_3)_2$ and $La_2O_2CO_3$ gave us indications that $LaFeO(CO_3)_2$ and $LaFeO_2CO_3$ were the most possible intermediate products in the thermal decomposition route.

3.3. Formation Mechanism of the Hollow Spheres. To investigate the formation mechanism of the hollow sphere with a porous shell, time-dependent hydrothermal experiments were carried out with a starting concentration of citric acid of 150 mM. The reaction time was began once the temperature reached 180 °C. After hydrothermal treatment for 1 h, the brown precipitates were formed and the solution color changed from dark yellow to light yellow. The SEM and TEM images of the brown precipitates are shown in Figures 5a and 5b, from which it can be seen that the diameters of these spheres are 2−5 μm and their surfaces are mostly smooth. The diameters of these complex spheres did not change, even after 3 h of reaction time, while the surface was corroded and many pores 20 nm in diameter were formed (see Figures 5c and 5d), which indicated that the digestive ripening process was taking place from the surface. By further increasing the reaction time to 12 h, the pore diameters enlarged (Figure 5e); at the same time, some yolk−shell structures were formed (see Figure 5f). Finally, the core was completely dissolved and the hollow spheres were formed after being reacted for 24 h (see Figure 1b). By extending

(16) (a) Todorovsky, D. S.; Todorovska, R. V.; Groudeva-Zotova, St. *Mater. Lett.* **2002**, *55*, 41. (b) Bernard, C.; Durand, B.; Verelst, M.; Lecante, P. *J. Mater. Sci.* **2004**, *39*, 2821. (c) da Silva, M. F. P.; Matos, J. R.; Isolani, P. C. *J. Therm. Anal. Calorim.* **2008**, *94*, 305. (d) Petrova, N.; Todorovsky, D.; Mitov, I.; Tyuliev, G. *J. Rare Earth* **2008**, *26*, 307.

(17) Navarro, M. C.; Pannunzio-Miner, E. V.; Pagola, S.; Inés Gómez, M.; Carbonio, R. E. *J. Solid-State Chem.* **2005**, *178*, 847.

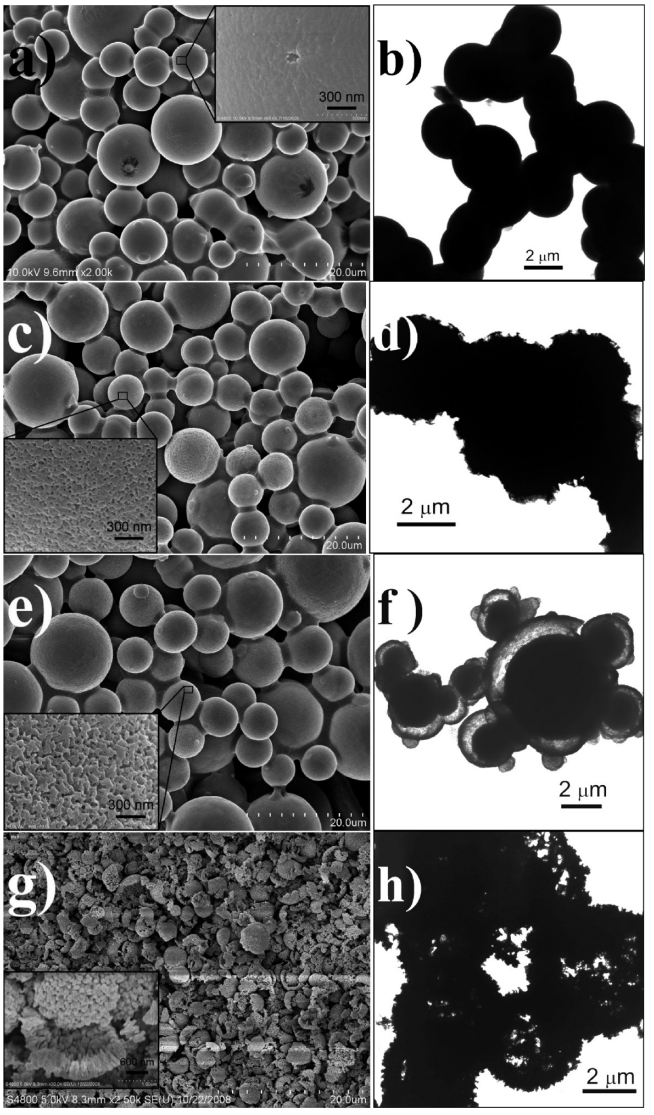

Figure 5. (a, c, e, and g) FESEM images and (b, d, f, and h) TEM images of the samples obtained after hydrothermal treatment for different times: (a) 1, (c) 3, (e) 12, and (g) 48 h. Panels (b), (d), (f), and (h) are TEM images corresponding to panels (a), (c), (e), and (g), respectively.

the reaction time to 48 h, hollow spheres collapsed to pieces (see Figure 5g). From the magnified image in the inset of Figure 5g, one could see that the shell is composed of nanoparticles and small channels exist among them. The TEM image shows that several hollow spheres left were deeply corroded and bigger holes (several hundred nanometers in diameter) existed on their surface (see Figure 5h).

The time-dependent hydrothermal process was also traced by ICP-AES. The concentrations of Fe^{3+} and La^{3+} in the supernatant at each hydrothermal treating time were recorded (see Table 4). The concentration of Fe^{3+} in the supernatant decreases rapidly in the first hour and increases slowly after that, whereas that of La^{3+} decreases gradually in 24 h, then increases slowly. The concentration of Fe^{3+} in the supernatant decreases more rapidly than that of La^{3+} at the beginning of hydrothermal treating. This indicates that the iron citrate complex was formed more quickly than the lanthanum citrate

Table 4. Concentration of Fe^{3+} and La^{3+} Ions in the Supernatant Obtained after Hydrothermal Treating for Different Times When the Starting Concentration of Citric Acid is 150 mM

	0.5 h	1.0 h	3.0 h	6.0 h	12.0 h	24.0 h	48.0 h
Fe^{3+} (mM)	0.456	0.188	0.524	2.47	2.74	3.23	5.46
La^{3+} (mM)	7.25	6.75	5.13	3.87	3.06	2.97	5.34

complex. The consequent increasing of both concentrations of Fe^{3+} (after 3 h) and La^{3+} (after 24 h) in the supernatant is the result of a digestive ripening process. Although the concentrations of Fe^{3+} and La^{3+} in the supernatant change with the time after being reacted for 12 h, their ratios are almost the same, which indicates the achievement of equivalent amounts of iron and lanthanum are maintained in the complex precursor after 12 h.

On the basis of the above experimental results, the formation mechanism of the La−Fe citrate complex hollow spheres is proposed as a digestive ripening process[18] by citric acid. At the beginning, the La−Fe citrate complex was formed and precipitated rapidly to form solid spheres in the hydrothermal conditions. From Table 4, it can be seen that the decreasing rate of the concentration of both Fe^{3+} and La^{3+} ions are quite different, which means that the iron citrate complex was formed more quickly than the lanthanum citrate complex, so the inner nucleus was mainly composed of the iron citrate complex. With the reaction going on, the concentration of Fe cations decreases rapidly; therefore, the formation rate of the iron citrate complex also decreases and grdually becomes close to that of the lanthanum citrate complex. So, there is a concentration gradient of Fe^{3+} and La^{3+} cations in the La−Fe citrate complex solid spheres at the early stage of the reaction. However, the reaction ultimately will reach the thermodynamic equilibrium concentration, that is, the La:Fe ratio is 1:1 in the final La−Fe citrate complex under hydrothermal conditions with 150 mM citric acid used. As can be seen in Table 4, the concentration of Fe^{3+} in solution begins to increase after reaction for 1 h, which indicates that the digestive ripening process begins under a thermodynamic driving force, whereas the concentration of La^{3+} in solution still decreases until the reaction has continued for 24 h. These results clearly show that excess iron citrate complex in the microspheres starts to be dissolved after reaction for 1 h, whereas the lanthanum citrate complex starts to dissolve after 24 h of reaction, which makes the concentration of La^{3+} and Fe^{3+} cations reach equivalent amounts when the reaction time lasts 24 h. In this process, the inner part of the microsphere is dissolved first, because it contains excessive iron citrate complex and its packing density also is looser than the outer part, because of the much faster aggregation rate. At the same time, the digestive process leads to the formation of many small pores on the surface, which would improve the transportation between the inside and the outside. These are the factors: the digestion process

(18) (a) Lin, X. M.; Wang, G. M.; Sorensen, C. M.; Klabunde, K. J. *J. Phys. Chem. B* **1999**, *103*, 5488. (b) Stoeva, S.; Klabunde, K. J.; Sorensen, C. M.; Dragieva, I. *J. Am. Chem. Soc.* **2002**, *124*, 2305. (c) Park, J.; Joo, J.; Kwon, S. G.; Jang, Y.; Hyeon, T. *Angew. Chem., Int. Ed.* **2007**, *46*, 4630.

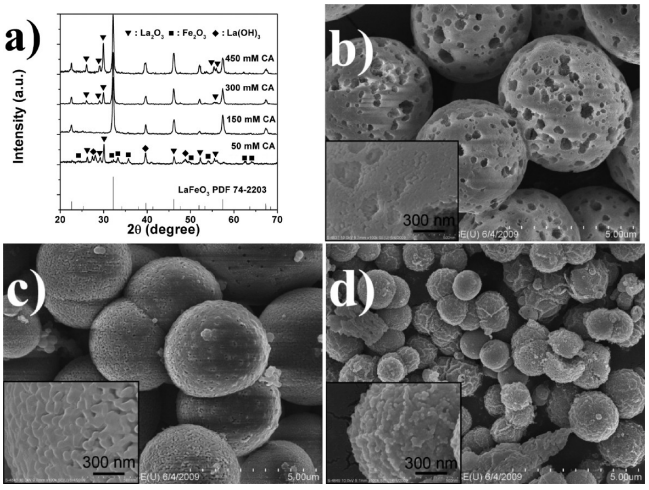

Figure 6. (a) XRD patterns of the products obtained from different concentration of citric acid (CA). FESEM images of the products obtained from different CA concentrations: (b) 300 mM, (c) 100 mM, and (d) 50 mM citric acid was used.

preferentially occurs in the inner part, and the hollow microspheres are gradually formed after reaction for 24 h. Extending the reaction time to 48 h made the pores on the shell bigger and the shell finally broken. Meanwhile, equivalent amounts of iron and lanthanum in the precursor complex are maintained by the thermodynamic equilibrium during the digestion process (Table 4). Using these La−Fe citrate complex hollow spheres as a precursor, $LaFeO_3$ hollow spheres with a porous structure were obtained after calcination in air.

3.4. Effect of Citric Acid. As discussed in Section 3.1, the concentration of citric acid is a key factor to the purity of the $LnFeO_3$. Using $LaFeO_3$ as an example, the effect of the concentration of citric acid on the purity and morphology of the products was discussed. XRD patterns of the products prepared at various concentrations of citric acid are shown in Figure 6a. From Figure 6a, we can see that a citric acid concentration of 150 mM is the optimum value to obtain the pure perovskite $LaFeO_3$: more or less than this value will lead to the generation of impurities. For example, when a citric acid concentration of 50 mM was used, no $LaFeO_3$ formed, but La_2O_3, Fe_2O_3, and a small amount of $La(OH)_3$ were found in the products. By increasing the concentration of citric acid to 300 mM and 450 mM, the main impurity is La_2O_3, which increases as the acid concentration increases. These experiment results are in good accordance with the diagram in Figure 2 and the ICP-AES results in Table 1. When the concentration of citric acid was 50 mM, the amount of iron citrate complex (25 mM) was larger than that of lanthanum citrate complex (16 mM) in the precursor. The unequal amount of iron and lanthanum ions in the La−Fe citrate complex made the phase separation happen during calcination; therefore, the main products were La_2O_3 and Fe_2O_3, whereas the present of $La(OH)_3$ was attributed to incomplete decomposition. When the concentration of citric acid was more than 150 mM, the acidity of the solution was quite high, and the pH values calculated were 1.80 and 1.75 for the concentrations of 300 mM and 450 mM, respectively. In previous studies, low pH value and excess of citrate would promote the depolymerization of ferric citrate polymers and the formation of soluble monomer.[19] This can be confirmed by the ICP-AES results in Table 1, from which it can be seen that the more citric acid used, the more iron was found in the supernatant. Therefore, the impurity of La_2O_3 appears in the final products.

The citric acid concentration also has great influence on the pore structure of the $LaFeO_3$ hollow spheres. As shown in Figure 6b, when 300 mM of citric acid was used, many big pores 200−600 nm in diameter were present on the surfaces of those hollow spheres, indicating that the spheres were deeply corroded in the stronger acidic solution. By decreasing the concentration of citric acid to 100 mM, there are no big pores but mesopores were present among the nanoparticles on the shells of the spheres (see Figure 6c). With the concentration of citric acid further decreasing, the nanoparticles packed closely and no obvious pores can be seen on the surfaces of the spheres (Figure 6d). The above results gave further evidence that the pores resulted from the digestion of the La−Fe citrate complex by citric acid.

This hydrothermal method can be easily extended to fabricate other $LnFeO_3$ spheres. The XRD patterns of all of the other 12 $LnFeO_3$ compounds are shown in Figures 7, from which we can see that all of these $LnFeO_3$ compounds have high purity and no impurities such as Ln_2O_3, $Ln_3Fe_5O_{12}$, or Fe_2O_3 could be found (every XRD pattern of the product was compared with the standard card in Figure S2 in the Supporting Information). The purity of these $LnFeO_3$ obtained was further confirmed by the EDS results (see Figure S3 in the Supporting Information), in which the Ln:Fe:O atomic ratio is near 1:1:3 and agrees well with the calculated value from its formula. The citric acid concentration also plays a critical role in the formation of pure $LnFeO_3$, and the optimum concentrations of citric acid are different for different lanthanide solutions, because the stability constants vary from complex to complex. From Figure S4 in the Supporting Information, we can see that the diagrams of the species distribution for light, median, and heavy rare-earth elements are quite different, because the stability constants increase as the atomic number of the lanthanide increases. The equivalent point of Ln and Fe citrate complexes moves toward the lower citric acid concentration. For example, for all heavy lanthanides, the citrate complex with Fe:Ln = 1:1 is formed when the concentration citric acid is >50 mM. The experimental optimum citric acid concentrations used for each lanthanide are slightly higher than the calculated values from Figure 2 and Figure S4 in the Supporting Information (see Table 5); however, the varying trends of both values are the same, viz, the value decreases as the atomic number increases for the light and median rare-earth elements (La−Sm,

(19) (a) Spiro, T. G.; Pape, L.; Saltman, P. *J. Am. Chem. Soc.* **1967**, *89*, 5555. (b) Spiro, T. G.; Pape, L.; Saltman, P. *J. Am. Chem. Soc.* **1967**, *89*, 5559. (c) Silva, A. M. N.; Kong, X.; Parkin, M. C.; Cammack, R.; Hider, R. C. *Dalton Trans.* **2009**, 8616.

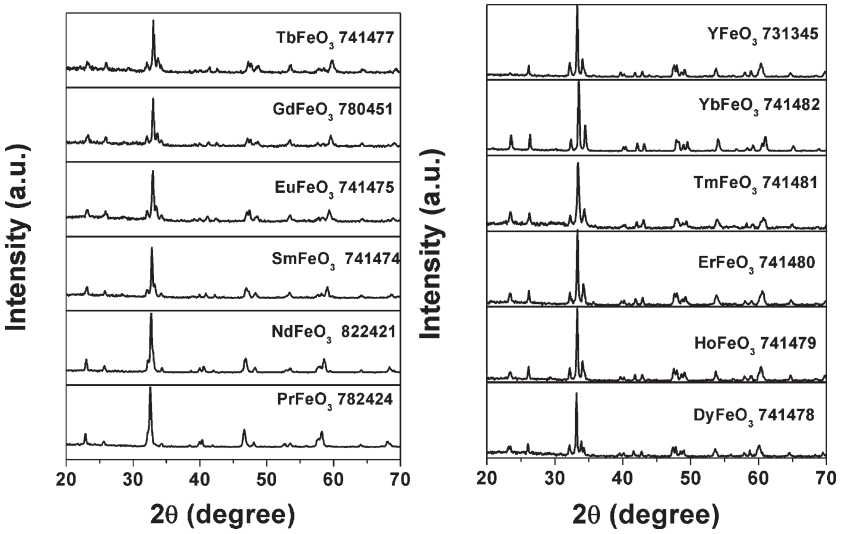

Figure 7. XRD patterns of $LnFeO_3$ (Ln = Pr−Yb, Y) hollow and solid microspheres obtained by hydrothermal reaction.

Table 5. Optimum Amount of Citric Acid Used for Synthesis of Each $LnFeO_3$ Obtained from Experimental Results and from Figure 2, Figure S4 in the Supporting Information, and the BET Surface Area Value of Each $LnFeO_3$

element	La	Pr	Nd	Sm	Eu	Gd	Tb
diagram results (mM)	150	100	90	80		70	60
experimental results (mM)	150	120	100	90	90	85	80
BET surface area (m^2/g)	49.3	33.4	37.2	30.2	32.3	31.3	29.7

element	Dy	Ho	Er	Tm	Yb	Y
diagram results (mM)	50	50	50	50	50	50
experimental results (mM)	70	70	70	70	70	70
BET surface area (m^2/g)	18.3	17.4	11.2	12.1	10.7	13.1

Eu−Dy), whereas the value remains almost constant for the heavy rare-earth elements (Y, Ho−Yb), which is parallel to the stability of lanthanide citrate complexes increasing with increasing atomic number.

The morphologies of various $LnFeO_3$ spheres are shown in Figure S5 in the Supporting Information. The morphological evolvement was similar to that of $LaFeO_3$ microspheres discussed above. With decreasing citric acid concentration, the pore size among the nanoparticles on the surface of the spheres becomes smaller. The $LnFeO_3$ spheres of heavy rare-earth elements (Dy−Yb, Y) are solid and have a compact surface, because the citric acid concentration that is required for pure $LnFeO_3$ is < 80 mM, which is not strong enough to digest the inner part or the surface of the spheres. As a result, the Brunauer−Emmett−Teller (BET) surface areas of $LnFeO_3$ spheres decreased from La to Yb (see Table 5). The nitrogen adsorption and desorption isotherms of $LaFeO_3$ hollow spheres are shown in Figure S6 in the Supporting Information. The isotherm can be categorized as Type IV with a distinct hysteresis loop observed in the range of 0.3−1.0 P/P_0. The BET surface area of the as-obtained $LaFeO_3$ hollow sphere is 49.3 m^2/g, which is much larger than that of $LaFeO_3$ nanoparticles obtained via other methods.[9−12] The Barrett−Joyner−Halenda (BJH) analyses show that the hollow spheres possess two types of pore distribution, with average pore sizes of ca. 30−80 nm and 100−300 nm (inset of Figure S6 in the Supporting Information); the former was attributed to the mesopores among the particles, and the latter was attributed to macropores on the surface.

3.5. Catalytic Performance of $LnFeO_3$ Microspheres for NO Reduction by CO. To investigate the potential application in the elimination of waste gas by pure-phase perovskite-structure $LnFeO_3$ microspheres, a mixture gas with NO:CO:He = 5:10:85 (volume ratio) was used as simulated waste gas. The conversion of NO and selectivity of N_2 and N_2O over $LaFeO_3$ hollow spheres are shown in Figure 8a. It can be seen that the catalytic activity of $LaFeO_3$ hollow spheres increases rapidly when the reaction temperature exceeds 225 °C, and the main product of the catalytic reduction reaction is N_2O when the reaction temperature is < 225 °C. Both of the NO conversion and N_2 selectivity increase as the temperature increases and reach $> 90\%$ at 325 °C; complete conversion with 100% N_2 selectivity is achieved at 350 °C. In recently described reports, with a comparable gas hourly space velocity (GHSV), the complete conversion was achieved at ~300 °C over noble-metal catalysts[20] and 350−450 °C over transition-metal composite-oxide catalysts.[21]

The NO conversion and N_2 selectivity over $LaFeO_3$ and the other 12 $LnFeO_3$ sphere catalysts is also shown in

(20) (a) Cónsul, J. M. D.; Costilla, I.; Gigola, C. E.; Baibich, I. M. *Appl. Catal., A* **2008**, *339*, 151. (b) Inomata, H.; Shimokawabe, M.; Kuwana, A.; Arai, M. *Appl. Catal., B* **2008**, *84*, 783. (c) Zhu, H.; Kim, J.-R.; Ihm, S.-K. *Appl. Catal., B* **2009**, *86*, 87. (d) Ilieva, L.; Pantaleo, G.; Nedyalkova, R.; Sobczak, J. W.; Lisowski, W.; Kantcheva, M.; Venezia, A. M.; Andreeva, D. *Appl. Catal., B* **2009**, *90*, 286.

(21) (a) Belessi, V. C.; Trikalitis, P. N.; Ladavos, A. K.; Bakas, T. V.; Pomonis, P. J. *Appl. Catal., A* **1999**, *177*, 53. (b) Peter, S. D.; Garbowski, E.; Perrichon, V.; Primet, M. *Catal. Lett.* **2000**, *70*, 27. (c) Zhu, J.; Zhao, Z.; Xiao, D.; Li, J.; Yang, X.; Wu, Y. *J. Mol. Catal. A* **2005**, *238*, 35. (d) Zhang, R.; Villanueva, A.; Alamdari, H.; Kaliaguine, S. *J. Mol. Catal. A* **2006**, *258*, 22. (e) Liu, L.; Chen, Y.; Dong, L.; Zhu, J.; Wan, H.; Liu, B.; Zhao, B.; Zhu, H.; Sun, K.; Dong, L.; Chen, Y. *Appl. Catal., B* **2009**, *90*, 105. (f) de Lima, R. K. C.; Batista, M. S.; Wallau, M.; Sanches, E. A.; Mascarenhas, Y. P.; Urquieta-González, E. A. *Appl. Catal., B* **2009**, *90*, 441.

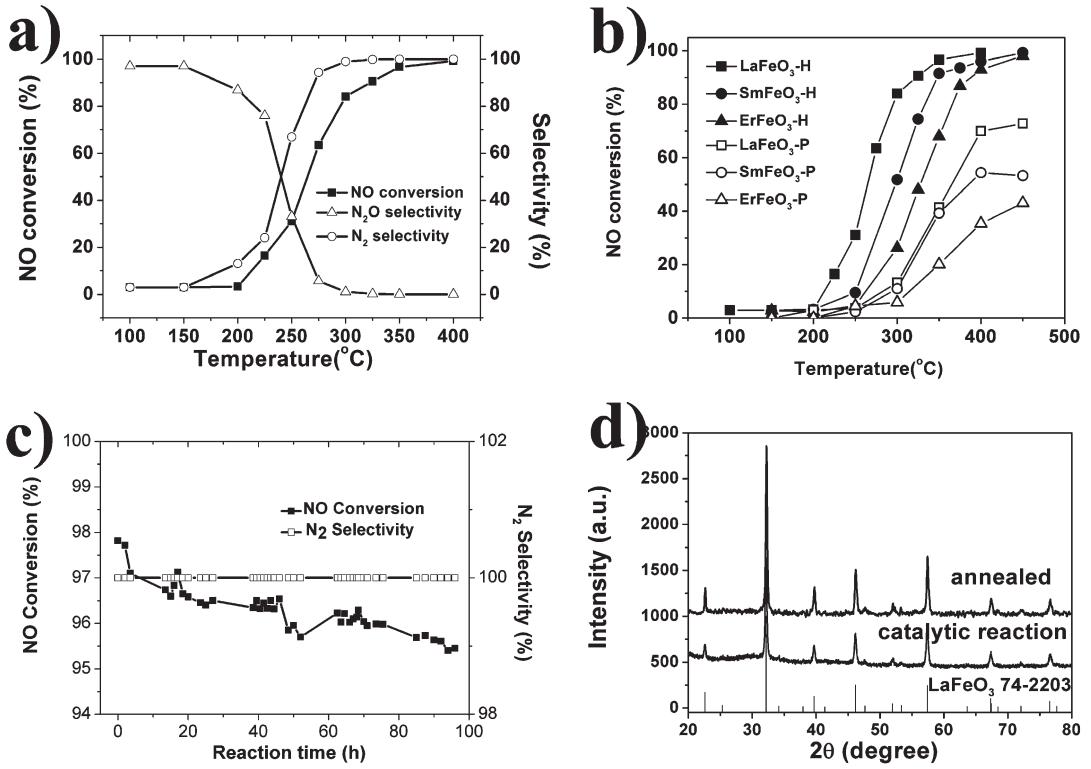

Figure 8. (a) NO conversion (%), N_2 selectivity (%), and N_2O selectivity (%) over $LaFeO_3$ hollow spheres as a function of reaction temperatures; (b) NO conversion (%) over three types of $LnFeO_3$ synthesized via Pechini process ($LnFeO_3$−P) and hydrothermal process ($LnFeO_3$−H), as a function of reaction temperatures; (c) lifetime test over $LaFeO_3$ hollow spheres for 96 h at 400 °C; and (d) XRD pattern of $LaFeO_3$ hollow spheres collected after NO + CO reaction for 96 h and annealing at 1000 °C in air.

Figure S7 in the Supporting Information, from which it could be found that the $LnFeO_3$ made of light and median rare-earth elements (Ln = La, Pr−Tb) usually had better catalytic activity. For example, the NO conversion was 10%−50% at 250 °C and >90% at a temperature of 350 °C; whereas for the $LnFeO_3$ made of heavy rare-earth elements (Ln = Dy−Yb, Y), NO conversion is <10% at 250 °C, merely 60%−80% at 350 °C, and almost 90% at a reaction temperature of 450 °C or even 500 °C. Previous works have showed that, in perovskite-type oxides with the formula ABO_3, the B-site cation was considered to be responsible for the catalytic activity, whereas the A-site cation was considered to be responsible for the thermal stability.[22] Since the A-site cations in $LnFeO_3$ were rare-earth elements with the same valences and close ionic radii, the difference between these two groups of $LnFeO_3$ might be mainly related to their BET surface area, which is an important factor in the gas-phase catalytic reaction. The porous shell with the larger surface area can offer more reactive sites and improve the transportation of the reactant and product. Therefore, it is reasonable that $LnFeO_3$ hollow spheres with a porous shell have better catalytic performance.

The three types of $LnFeO_3$ nanoparticles composed of light, median, and heavy rare-earth elements ($LaFeO_3$, $SmFeO_3$, and $ErFeO_3$) were also synthesized via the Pechini process.[11c] FESEM images showed that they were composed of particles 50−300 nm in diameter with irregular morphology (see Figure S8 in the Supporting Information). The BET surface areas of these $LnFeO_3$ were in the range of 5−8 m^2/g, which were in accordance with previous results.[11d−g] The NO conversion over three types of $LnFeO_3$ synthesized via both the Pechini process ($LnFeO_3$−P) and the hydrothermal process ($LnFeO_3$−H) is shown in Figure 8b. It can be seen that, under the same catalytic conditions, the NO conversion over $LnFeO_3$−P is relatively lower than that over $LnFeO_3$−H. Briefly, the catalytic activity of $LnFeO_3$−P appears when the reaction temperature exceeds 300 °C, and almost 80% NO conversion at 450 °C in the case of $LaFeO_3$−P. The NO conversion over $SmFeO_3$−P and $ErFeO_3$−P is much lower: only 40%−50%, even when the reaction temperature reached 450 °C. These results further confirmed that the porous structure with larger BET surface area is of benefit to this gas-phase catalytic reaction.

In addition to the excellent catalytic performance, the thermal and chemical stabilities of the $LnFeO_3$ hollow spheres are also quite good. The lifetime test of $LaFeO_3$ hollow spheres at 400 °C was carried out (Figure 8c), from which it can be seen that the selectivity of N_2 was 100% and the conversion of NO was almost constant (>95.5%) during the reaction lasting for 96 h. XRD pattern (Figure 8d) and FESEM image (see Figure S9a in the Supporting Information) of $LaFeO_3$ hollow spheres after reaction for the 96 h showed no obvious change in the structure or the crystal phase. The $LaFeO_3$ hollow

(22) (a) Tabata, K.; Misono, M. *Catal. Today* **1990**, *8*, 249. (b) Viswanathan, B. *Catal. Rev.−Sci. Eng.* **1992**, *34*, 337. (c) Peña, M. A.; Fierro, J. L. G. *Chem. Rev.* **2001**, *101*, 1981. (d) Mawdsley, J. R.; Krause, T. R. *Appl. Catal., A* **2008**, *334*, 311.

spheres were also annealed at 1000 °C in air and were also observed to have little change in XRD pattern (Figure 8d) or FESEM image (Figure S9b in the Supporting Information). These thermal and chemical stabilities make the $LnFeO_3$ hollow spheres very suitable for long-time running and reuse.

4. Conclusions

Pure-phase $LnFeO_3$ (Ln = La, Pr−Tb) hollow spheres with a porous shell and solid spheres (Ln = Dy−Yb, Y) were successfully synthesized using Ln-Fe citrate complex as a precursor. The composition and the thermal decomposition process of the Ln-Fe citrate complex were investigated systematically. The formation mechanism of the Ln-Fe citrate complex hollow spheres is proposed as an acidic digestion ripening process. Therefore, to control the ratio of Ln^{3+} and Fe^{3+} in the Ln-Fe citrate complex precursor and also in the final product, a diagram of reaction species distribution was constituted. From the diagram, the reaction parameters can be selected; therefore, the preparation of the pure-phase $LnFeO_3$ with perovskite structure becomes quite easy. By simply adjusting the citric acid concentration, pure-phase $LnFeO_3$ compounds of 13 rare-earth elements with perovskite structure could be obtained. The optimum citric acid concentration calculated from the diagram of species distribution is very coincident with the experimental value. Also, the citric acid concentration had great influence on the pore structure of the $LnFeO_3$ spheres. Stronger acidity of the reaction solution leads to the formation of hollow spheres with a porous shell and, therefore, a larger BET surface area in the group of light and median rare-earth elements (Ln = La,Pr−Tb). All 13 pure-phase $LnFeO_3$ microspheres showed excellent catalytic performance for the NO + CO reaction at 200−500 °C, whereas $LnFeO_3$ (Ln = La, Pr−Tb) hollow spheres with a porous shell were even better than the solid spheres with a compact shell made of heavy rare-earth elements (Ln = Dy−Yb, Y). Because of their relatively larger BET surface area, $LnFeO_3$ synthesized via the hydrothermal process had better catalytic activity than those from the Pechini process. Combined with the excellent thermal and chemical stabilities, the $LnFeO_3$ hollow spheres may have promise application in waste gas treatment in the future.

Acknowledgment. This work was financially supported by National Basic Research Program (973 program, 2007CB936302) and the National Natural Science Foundation of China (NNSFC), under Major Project No. 90606005.

Supporting Information Available: The details of stability constants used in this work; more XRD and EDS results; diagrams of the species distribution of Fe and Ln ions (Pr−Yb, Y) in citric acid solution; N_2 adsorption−desorption isotherm and BJH pore-size distribution plot of $LaFeO_3$ hollow spheres; NO conversion and N_2 selectivity over 13 $LnFeO_3$ compounds; FESEM images of $LnFeO_3$ spheres (Ln = Pr−Yb, Y) synthesized via the hydrothermal process and the Pechini process; and FESEM images of $LaFeO_3$ hollow spheres after the NO + CO reaction for 96 h and annealing at 1000 °C in air. This material is available free of charge via the Internet at http://pubs.acs.org.